Multiphase lattice Boltzmann flux solver for incompressible multiphase flows with large density ratio

Y. Wang [a], C. Shu [a,*], H.B. Huang [b], C.J. Teo [a]

[a] *Department of Mechanical Engineering, National University of Singapore, 10 Kent Ridge Crescent, Singapore 119260, Singapore*
[b] *Department of Modern Mechanics, University of Science and Technology of China, Hefei, Anhui 230026, China*

A R T I C L E   I N F O

A B S T R A C T

A multiphase lattice Boltzmann flux solver (MLBFS) is proposed in this paper for incompressible multiphase flows with low- and large-density-ratios. In the solver, the flow variables at cell centers are given from the solution of macroscopic governing differential equations (Navier–Stokes equations recovered by multiphase lattice Boltzmann (LB) model) by the finite volume method. At each cell interface, the viscous and inviscid fluxes are evaluated simultaneously by local reconstruction of solution for the standard lattice Boltzmann equation (LBE). The forcing terms in the governing equations are directly treated by the finite volume discretization. The phase interfaces are captured by solving the phase-field Cahn–Hilliard equation with a fifth order upwind scheme. Unlike the conventional multiphase LB models, which restrict their applications on uniform grids with fixed time step, the MLBFS has the capability and advantage to simulate multiphase flows on non-uniform grids. The proposed solver is validated by several benchmark problems, such as two-phase co-current flow, Taylor–Couette flow in an annulus, Rayleigh–Taylor instability, and droplet splashing on a thin film at density ratio of 1000 with Reynolds numbers ranging from 20 to 1000. Numerical results show the reliability of the proposed solver for multiphase flows with high density ratio and high Reynolds number.

© 2014 Elsevier Inc. All rights reserved.

1. Introduction

Multiphase flows of incompressible fluids are ubiquitous in nature and of great interest in both science and engineering applications [1–4]. To effectively simulate such flows, various numerical methods, including volume of fluid (VOF) method [5], level set approach [6], front tracking method [7] and diffuse interface methods [8,9] have been proposed. Among them, the lattice Boltzmann method (LBM) [10,11] received more and more attention in recent years. As a mesoscopic method with microscopic models, LBM has an instinct kinetic nature and only involves simple algebraic manipulations of streaming-collision processes. Due to these attractive features, many multiphase lattice Boltzmann (LB) models [12–25] have been developed for simulating multiphase flows with low- and large-density-ratios [26–30] during the past two decades.

---

* Corresponding author.
  E-mail address: mpeshuc@nus.edu.sg (C. Shu).

The early attempts in the 1990s were focused on the development of reliable multiphase LB models [13–17]. The first model, also known as color-gradient model, was perhaps proposed by Gunstensen et al. [13]. This model introduces an additional two-phase collision step to control interfacial interactions caused by surface tension. Later, Shan and Chen [14,15] developed a potential multiphase LB model for multiphase and multi-component flows by introducing inter-particle interaction forces. Although it cannot satisfy the momentum conservation law at a local position [14], the Shan–Chen (SC) LB model has attained much popularity due to its overall accuracy and ease for implementation. Unlike the color-gradient model, Swift et al. [16] introduced a thermodynamically consistent multiphase LB model based on the free-energy functional, which successfully satisfies the momentum conservation law. Unfortunately, due to the intrinsic density variation across the interface in multiphase flows, this model lacks Galilean invariance which plagues its wide application. He et al. [17] proposed a double-distribution-functions (DDFs) model based on the kinetic theory. One of the DDFs is adopted for the evolution of pressure and velocity field and the other DDF is used to capture the interface of different phases.

Due to numerical instability, these multiphase LB models [13–17] restrict their applications for multiphase flows with low- and/or moderate-density-ratio. There were also several attempts to develop multiphase LB models for multiphase flows with large-density-ratio [18–23] during the past decade. A projection-like LB model [19] was proposed by enforcing the incompressibility condition through a pressure-correction process. This model has been applied for binary flows with density ratio up to 1000. However, the pressure correction step [19] spoils the simplicity and efficiency of the LBM. To get a more effective model, Lee and Lin [20] and Lee and Liu [21] proposed a stable discretization algorithm for LBE on the basis of the DDF model [17]. Their method introduces the thermodynamic pressure tensor in a specific form and directional derivatives to stabilize the solution process. Zheng et al. [22] later proposed an improved LB model, which is able to accurately recover Cahn–Hilliard equation, i.e., the interface capturing equation. Yan and Zu [23] combined the projection-like LB model [19] and the free energy model [24,25] to simulate multiphase flows with large density ratio and partial wetting surfaces.

The multiphase LB models mentioned above [12–25] share the same advantages of LBM, such as intrinsic kinetic nature, simple streaming and collision processes, and explicit feature. On the other hand, the disadvantages of the LBM are also kept by these models, such as limitation to uniform mesh, tie-up between the time step and the mesh spacing, and complex implementation of boundary conditions. To eliminate the drawbacks of the LBM, a lattice Boltzmann flux solver (LBFS) for single phase flows has been recently presented [31–33]. LBFS is a finite volume solver for direct update of the macroscopic flow variables at cell centers. The single-phase LB model is applied locally at the cell interface to reconstruct the viscous and inviscid fluxes simultaneously. Due to the local application of the LBM, LBFS not only successfully eliminates the previously mentioned drawbacks of the LBM but also effectively combines the advantages of the Navier–Stokes solvers and the LBM.

In this series of work, we aim to develop a multiphase lattice Boltzmann flux solver (MLBFS) for effective simulation of incompressible multiphase flows with both low and large density ratios. As mentioned above, the multiphase LB model is usually very complicated due to consideration of forcing terms in the model itself. This drawback can be overcome in the developed MLBFS since LB model is only applied at each cell interface locally. To be specific, we start from the macroscopic governing differential equations recovered by conventional multiphase LB models, which will be solved by the finite volume method. Then we consider the standard LBE without forcing terms and perform the Chapman–Enskog expansion analysis. From the analysis, we can establish relationships between fluxes in the governing differential equations and density distribution functions in the standard LBE. These relationships will be used to evaluate fluxes at each cell interface during finite volume discretization of governing differential equations. The forcing terms in the governing differential equations are directly treated by the finite volume method. Since the standard LB model is applied locally at each interface, and flow variables at cell centers are given directly from the solution of macroscopic governing equations, the physical boundary conditions can be directly implemented. Apart from the flow field, the evolution of the interface is modeled by the Cahn–Hilliard equation, which is solved by the fifth-order upwind scheme. Overall, the MLBFS can be effectively applied for multiphase flows with large density ratios on non-uniform grids, and retains the simplicity and advantages of the standard LBM. In addition, as compared with the conventional N–S solver, the present method is also much simpler and more flexible for applications on body-fitted grids by avoiding the application of staggered grid and the pressure–velocity coupling. The reliability and capability of the MLBFS will be validated by its application to simulate several test examples such as the two-phase co-current flows with density ratio up to 1000, Taylor–Couette flows in an annulus, droplet spreading on a flat plate, Rayleigh–Taylor instability and droplet splashing on a thin film.

2. Methodology

2.1. Governing equations

To show the governing equations of the MLBFS, the macroscopic Navier–Stokes (N–S) equations, recovered by the multiphase LB model [21], are described first. After that, the standard LBE model, which does not involve external forcing terms, will be analyzed by the multi-scale Chapman–Enskog expansion analysis. From the analysis, relationships between the fluxes in the governing differential equations and density distribution function in the standard LBE will be established. These relationships will then be incorporated into the final governing equations.
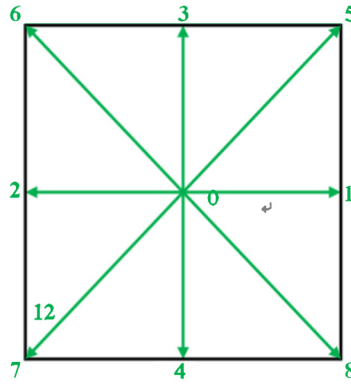
Fig. 1. The D2Q9 lattice velocity model.

2.1.1. Macroscopic Navier–Stokes (N–S) equations

The macroscopic governing equations, recovered by the multiphase LB model [21], can be written as:

$$\left(\frac{\partial p}{\partial t} + \boldsymbol{u} \cdot \nabla p\right) + \rho c_s^2 \nabla \cdot \boldsymbol{u} = 0, \tag{1a}$$

$$\frac{\partial \rho \boldsymbol{u}}{\partial t} + \nabla \cdot (\rho \boldsymbol{u} \otimes \boldsymbol{u}) = -\nabla p + \nabla\left[\mu \cdot \left(\nabla \boldsymbol{u} + (\nabla \boldsymbol{u})^T\right)\right] + \boldsymbol{F}_s, \tag{1b}$$

where ρ is the fluid density, $\boldsymbol{u}$ is the flow velocity, p is the pressure and $\boldsymbol{F}_s$ is the surface tension. Note that, in the recovery of Eq. (1), complicated external forcing terms are involved in the evolution equations of the conventional multiphase LB model [20,21]. The existence of these external forcing terms may introduce additional errors and spoil the simplicity of the LBM. To eliminate this drawback, the standard LBE without any external forcing terms is analyzed and applied to derive the governing equations of the MLBFS.

2.1.2. Standard lattice Boltzmann equation (LBE) and Chapman–Enskog expansion analysis

The standard LBE for multiphase flows of binary immiscible fluids can be written as:

$$f_\alpha(\boldsymbol{r} + \boldsymbol{e}_\alpha \delta_t, t + \delta_t) = f_\alpha(\boldsymbol{r}, t) + \frac{f_\alpha^{eq}(\boldsymbol{r}, t) - f_\alpha(\boldsymbol{r}, t)}{\tau}, \quad \alpha = 0, 1, \ldots, N \tag{2}$$

where $\boldsymbol{r} = (x, y)$ represents a physical location, f_α is the particle distribution function, τ is the single relaxation parameter; δ_t is the streaming time step and $\boldsymbol{e}_\alpha$ is the particle velocity in the α direction; N is the number of discrete particle velocities. f_α^{eq} is the equilibrium state of f_α given as follows:

$$f_\alpha^{eq}(\boldsymbol{r}, t) = w_\alpha\left[p + \rho c_s^2\left(\frac{\boldsymbol{e}_\alpha \cdot \boldsymbol{u}}{c_s^2} + \frac{(\boldsymbol{e}_\alpha \cdot \boldsymbol{u})^2 - (c_s|\boldsymbol{u}|)^2}{2c_s^4}\right)\right], \tag{3}$$

where the coefficients w_α and the sound speed c_s depend on the lattice velocity model. There are a number of lattice velocity models for the two-dimensional (2D) cases. The most popular lattice velocity model is D2Q9 model shown in Fig. 1, which can be written as

$$\boldsymbol{e}_\alpha = \begin{cases} 0 & \alpha = 0, \\ (\cos[(\alpha - 1)\pi/2], \sin[(\alpha - 1)\pi/2])c & \alpha = 1, 2, 3, 4, \\ \sqrt{2}(\cos[(\alpha - 5)\pi/2 + \pi/4], \sin[(\alpha - 5)\pi/2 + \pi/4])c & \alpha = 5, 6, 7, 8. \end{cases} \tag{4}$$

Here $c = \delta_x/\delta_t$, δ_x is the lattice spacing. For the D2Q9 model, the coefficients w_α and the sound speed c_s are given as $w_0 = 4/9$, $w_1 = w_2 = w_3 = w_4 = 1/9$ and $w_5 = w_6 = w_7 = w_8 = 1/36$, $c_s = c/\sqrt{3}$.

The particle distribution functions f_α and their equilibrium states f_α^{eq} satisfy the mass and momentum conservation laws at any physical location:

$$p = \sum_{\alpha=0}^{N} f_\alpha^{eq} = \sum_{\alpha=0}^{N} f_\alpha, \tag{5a}$$

$$\rho \boldsymbol{u} c_s^2 = \sum_{\alpha=0}^{N} f_\alpha^{eq} \boldsymbol{e}_\alpha = \sum_{\alpha=0}^{N} f_\alpha \boldsymbol{e}_\alpha. \tag{5b}$$

The multi-scale Chapman–Enskog expansion analysis to Eq. (2) gives the following equations (details are shown in Appendix A):

$$\frac{\partial p}{\partial t} + \nabla \cdot \left(\sum_{\alpha=0}^{N} \boldsymbol{e}_\alpha f_\alpha^{eq} \right) = 0, \tag{6a}$$

$$\frac{\partial \rho c_s^2 \boldsymbol{u}}{\partial t} + \nabla \cdot \Pi = 0, \tag{6b}$$

where Π is the momentum flux tensor defined by

$$\Pi_{\beta\gamma} = \sum_{\alpha=0}^{N} (\boldsymbol{e}_\alpha)_\beta (\boldsymbol{e}_\alpha)_\gamma \left[f_\alpha^{eq} + \left(1 - \frac{1}{2\tau} \right) f_\alpha^{neq} \right], \tag{7a}$$

$$f_\alpha^{neq} = -\tau \delta_t \left(\frac{\partial}{\partial t} + \boldsymbol{e}_\alpha \cdot \nabla \right) f_\alpha^{eq}. \tag{7b}$$

As shown in Appendix A, after some manipulations, the above equations can be rewritten as

$$\frac{\partial p}{\partial t} + \nabla \cdot \left(\rho c_s^2 \boldsymbol{u} \right) = 0, \tag{8a}$$

$$\frac{\partial \rho \boldsymbol{u}}{\partial t} + \nabla(\rho \boldsymbol{u} \otimes \boldsymbol{u}) = -\nabla p + \nabla \left[\mu \left(\nabla \boldsymbol{u} + (\nabla \boldsymbol{u})^T - \Pi^e / c_s^2 \right) \right], \tag{8b}$$

where

$$\Pi_{jk}^e = \frac{1}{\rho} \left(u_j \frac{\partial}{\partial x_k} + u_k \frac{\partial}{\partial x_j} \right) (p - \rho c_s^2), \tag{9}$$

$$\mu = \rho c_s^2 (\tau - 1/2)\delta_t. \tag{10}$$

It can be seen that both the mass and momentum equations of Eq. (8) recovered by the standard LBE deviates from the true N–S equations given by Eq. (1). Due to this discrepancy, the standard LBE model cannot be directly applied for simulation of multiphase flows. To accurately recover Eq. (1), the conventional multiphase LB models usually add complex external forcing terms into the LBE. As indicated earlier, the inclusion of external forcing terms may spoil the simplicity of the LBM and introduce additional errors. In addition, the compatibility conditions for mass and momentum conservations shown in Eq. (5) also become more complicated by including some gradient terms. To eliminate these drawbacks and effectively make use of the advantages of the standard LBE model, we can incorporate the relationships of the standard LBE model into the macroscopic governing equation (1).

2.1.3. Governing equations of MLBFS

By comparing Eq. (6) and Eq. (8), we can have the following relationships,

$$\rho \boldsymbol{u} c_s^2 = \sum_{\alpha=0}^{N} f_\alpha^{eq} \boldsymbol{e}_\alpha \tag{11a}$$

$$(\rho \boldsymbol{u} \otimes \boldsymbol{u}) + \nabla p - \mu \left(\nabla \boldsymbol{u} + (\nabla \boldsymbol{u})^T \right) = \left(\Pi - \mu \Pi^e \right) / c_s^2 \tag{11b}$$

Substituting Eq. (11) into Eq. (1) gives

$$\frac{\partial p}{\partial t} + \nabla \cdot \left(\sum_{\alpha=0}^{N} \boldsymbol{e}_\alpha f_\alpha^{eq} \right) + \boldsymbol{u} \cdot \nabla \left(p - \rho c_s^2 \right) = 0, \tag{12a}$$

$$\frac{\partial \rho \boldsymbol{u} c_s^2}{\partial t} + \nabla \cdot \left(\Pi - \mu \Pi^e \right) - \boldsymbol{F}_s c_s^2 = 0, \tag{12b}$$

where Π and Π^e are respectively shown in Eqs. (7) and (9). Note that in Eq. (12), the distribution function f_α is given by the standard LBE. Eq. (12) is the governing equation for the application of MLBFS. In the next section, we will discuss numerical discretization of Eq. (12) by using the finite volume method.
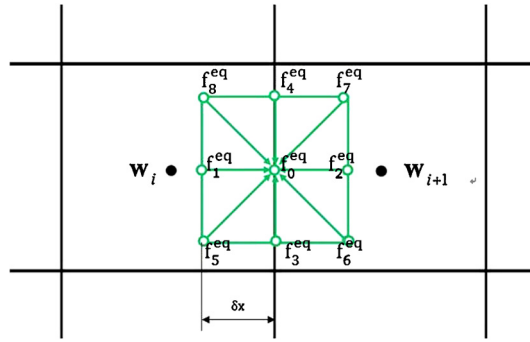
Fig. 2. Local reconstruction of LBE solution at cell interface, $\boldsymbol{W} = (p, \rho u, \rho v)$.

2.1.4. Finite volume discretization

A cell-centered finite volume method is applied in the MLBFS to solve Eq. (12) so that the flow variables ($\boldsymbol{W} = (p, \rho u c_s^2, \rho v c_s^2)$) can be marched in time at the cell centers. Integrating Eq. (12) over a control volume Ω_i, we have the following formula:

$$\frac{d\boldsymbol{W}_i}{dt} = -\frac{1}{\Delta V_i} \sum_k \boldsymbol{R}_k \Delta S_k + \boldsymbol{F}_E, \tag{13}$$

$$\boldsymbol{F}_E = \left(-\boldsymbol{u} \cdot \nabla(p - \rho c_s^2), c_s^2 F_{sx}, c_s^2 F_{sy}\right)^T, \tag{14}$$

where ΔV_i is the volume of Ω_i, and ΔS_k is the area of the kth control surface enclosed Ω_i. The detailed expression of the flux $\boldsymbol{R}_k$ at an interface depends on the lattice velocity model. The D2Q9 lattice model shown in Fig. 1 is applied here. If we define the distribution functions $f_\alpha^\wedge$ as

$$f_\alpha^\wedge = f_\alpha^{eq} + \left(1 - \frac{1}{2\tau}\right) f_\alpha^{neq}, \tag{15a}$$

$$f_\alpha^{neq} = -\tau \delta_t \left(\frac{\partial}{\partial t} + \boldsymbol{e}_\alpha \cdot \nabla\right) f_\alpha^{eq}, \tag{15b}$$

then the flux $\boldsymbol{R}_k$ can be written in detail as:

$$\boldsymbol{R}_k = \begin{bmatrix} [n_x(f_1^{eq} - f_3^{eq} + f_5^{eq} - f_6^{eq} - f_7^{eq} + f_8^{eq}) + n_y(f_2^{eq} - f_4^{eq} + f_5^{eq} + f_6^{eq} - f_7^{eq} - f_8^{eq})] \\ n_x(f_1^\wedge + f_3^\wedge + f_5^\wedge + f_6^\wedge + f_7^\wedge + f_8^\wedge - \mu \cdot \Pi_{11}^e) + n_y(f_5^\wedge - f_6^\wedge + f_7^\wedge - f_8^\wedge - \mu \cdot \Pi_{12}^e) \\ n_x(f_5^\wedge - f_6^\wedge + f_7^\wedge - f_8^\wedge - \mu \cdot \Pi_{21}^e) + n_y(f_2^\wedge + f_4^\wedge + f_5^\wedge + f_6^\wedge + f_7^\wedge + f_8^\wedge - \mu \cdot \Pi_{22}^e) \end{bmatrix}_k \tag{16}$$

where n_x and n_y are the x and y components of the unit outer normal vector on the kth control surface. In Eq. (15), τ is defined by the kinematic viscosity v:

$$v = c_s^2 \left(\tau_v - \frac{1}{2}\right) \cdot \delta_t. \tag{17}$$

To evaluate the flux $\boldsymbol{R}_k$ at the cell interface, the unknowns are $f_\alpha^\wedge$ and Π_{jk}^e according to Eq. (16). As shown in Eq. (9), Π_{jk}^e only includes the velocity and first order derivatives of the density and pressure. The numerical value of Π_{jk}^e can be easily calculated at the cell interface by discretizing these terms directly. The key issue, to evaluate the flux $\boldsymbol{R}_k$, is the evaluation of $f_\alpha^\wedge$ at an interface between two adjacent control volumes. Details of the evaluation procedure are given below.

2.1.5. Evaluation of $f_\alpha^\wedge$ at a cell interface by MLBFS

Consider an interface between two adjacent control volumes shown in Fig. 2. The evaluation of $f_\alpha^\wedge$ is performed at the middle point of the interface. According to Eq. (15), both the equilibrium density distribution functions f_α^{eq} and non-equilibrium density distribution functions f_α^{neq} are included in $f_\alpha^\wedge$. The evaluation procedure for f_α^{eq} and f_α^{neq} are illustrated respectively.

Through Taylor-series expansion to Eq. (15b) with the second order of accuracy, f_α^{neq} can be approximated by f_α^{eq} at the cell interface and its surrounding points:

$$f_\alpha^{neq}(\boldsymbol{r}, t) = -\tau \left[f_\alpha^{eq}(\boldsymbol{r}, t) - f_\alpha^{eq}(\boldsymbol{r} - \boldsymbol{e}_\alpha \delta_t, t - \delta_t)\right] \tag{18}$$

Here in Eq. (18), $\boldsymbol{r}$ represents the mid-point of an interface between two adjacent control volumes. Following the convention of the LBM and according to Eq. (3), $f_\alpha^{eq}(\boldsymbol{r} - \boldsymbol{e}_\alpha \delta_t, t - \delta_t)$ can be computed from ρ, $\boldsymbol{u}$ and p at $(\boldsymbol{r} - \boldsymbol{e}_\alpha \delta_t, t - \delta_t)$. As shown

in Fig. 2, if $\mathbf{r}_i$ and $\mathbf{r}_{i+1}$ are defined as the physical positions of the two cell centers respectively, ρ, $\mathbf{u}$ and p at the location $\mathbf{r} - \mathbf{e}_\alpha \delta_t$ can be calculated by interpolation with given flow properties at these cell centers. One possible interpolation formulation for ρ, $\mathbf{u}$ and p can be given as:

$$\psi(\mathbf{r} - \mathbf{e}_\alpha \delta_t, t - \delta_t) = \begin{cases} \psi(\mathbf{r}_i) + (\mathbf{r} - \mathbf{e}_\alpha \delta_t - \mathbf{r}_i) \cdot \nabla \psi(\mathbf{r}_i), & \text{when } \mathbf{r} - \mathbf{e}_\alpha \delta_t \text{ is in } \Omega_i \\ \psi(\mathbf{r}_{i+1}) + (\mathbf{r} - \mathbf{e}_\alpha \delta_t - \mathbf{r}_{i+1}) \cdot \nabla \psi(\mathbf{r}_{i+1}), & \text{when } \mathbf{r} - \mathbf{e}_\alpha \delta_t \text{ is in } \Omega_{i+1} \end{cases} \tag{19}$$

where ψ represents the flow variables ρ, $\mathbf{u}$ and p. After interpolation of these flow properties, $f_\alpha^{eq}(\mathbf{r} - \mathbf{e}_\alpha \delta_t, t - \delta_t)$ can be computed using Eq. (3).

The only left unknown is $f_\alpha^{eq}(\mathbf{r}, t)$. In a similar way to those for $f_\alpha^{eq}(\mathbf{r} - \mathbf{e}_\alpha \delta_t, t - \delta_t)$, $f_\alpha^{eq}(\mathbf{r}, t)$ can also be computed by ρ, $\mathbf{u}$ and p at $(\mathbf{r}, t)$ using Eq. (3). $p(\mathbf{r}, t)$ and $\rho(\mathbf{r}, t)\mathbf{u}(\mathbf{r}, t)$ can be constructed by the LBM solution as [31–33]:

$$p(\mathbf{r}, t) = \sum_{\alpha=0}^{N} f_\alpha^{eq}(\mathbf{r} - \mathbf{e}_\alpha \delta_t, t - \delta_t), \tag{20}$$

$$\rho(\mathbf{r}, t)\mathbf{u}(\mathbf{r}, t) c_s^2 = \sum_{\alpha=0}^{N} f_\alpha^{eq}(\mathbf{r} - \mathbf{e}_\alpha \delta_t, t - \delta_t)\mathbf{e}_\alpha, \tag{21}$$

$$\rho(\mathbf{r}, t) = \sum_{\alpha=0}^{N} w_\alpha \rho(\mathbf{r} - \mathbf{e}_\alpha \delta_t, t - \delta_t), \tag{22}$$

where, $f_\alpha^{eq}(\mathbf{r} - \mathbf{e}_\alpha \delta_t, t - \delta_t)$ has already been evaluated and w_α is the coefficient given in Eq. (3). Note that Eq. (22) has the second order of accuracy in space due to the isotropic property of the first rank lattice tensor. By applying Eqs. (3) and (20)–(22), $f_\alpha^{eq}(\mathbf{r}, t)$ can be calculated.

Once $f_\alpha^{eq}(\mathbf{r} - \mathbf{e}_\alpha \delta_t, t - \delta_t)$ and $f_\alpha^{eq}(\mathbf{r}, t)$ are obtained, f_α^{neq} can be computed by using Eq. (18) and then $f_\alpha^\wedge$ can be easily calculated by applying Eq. (15a).

Once $f_\alpha^\wedge$ and Π_{jk}^e are obtained, the flux at any interface can be evaluated according to Eq. (16). Then, the flow variables at the cell center can be updated by solving Eq. (13) with a well-known temporal scheme such as the third order TVD (Total Variation Diminishing) Runge–Kutta temporal scheme [34].

2.2. Cahn–Hilliard model for interface capture

In addition to the pressure evolution and momentum equations (12) for the pressure and velocity filed, the Cahn–Hilliard model is applied in this work to capture the interface of two incompressible immiscible fluids in multiphase flows. The governing equation of this model can be written as [21]:

$$\frac{\partial C}{\partial t} + \nabla \cdot (\mathbf{u}C) = M\nabla^2 \mu_C, \tag{23}$$

where C is noted as the volume fraction of heavier fluids in the range of [0, 1]; M is known as the constant mobility or diffuse flow rate; the local density ρ is taken as a linear composition of the heavier and lighter fluids (ρ_H and ρ_L) by the volume fraction C:

$$\rho = C\rho_H + (1 - C)\rho_L. \tag{24}$$

In Eq. (23), μ_C represents the chemical potential determined by the total free energy of fluid–fluid or fluid–wall interfaces.

$$F(C, \nabla C) = \int_V \left(E_0(C) + \frac{\kappa}{2}|\nabla C|^2 \right) dV + \int_S \varphi(C_S) dS, \tag{25}$$

where the bulk free energy can be defined by $E_0 = \beta C^2(C - 1)^2$ with a constant of β; κ is a fixed gradient parameter; $\varphi(C_s)$ represents the wall free energy per unit area. When an equilibrium state of the interface interactions is reached, the total free energy is minimized. With this condition, the chemical potential μ can be determined by:

$$\mu_C = \frac{\partial E_0}{\partial C} - \kappa \nabla^2 C = 2\beta C(C - 1)(2C - 1) - \kappa \nabla^2 C. \tag{26}$$

If the thickness of an interface ξ and the interfacial tension force σ are given, the constants β and κ in Eq. (26) can be determined by the following two equations:

$$\sigma = \sqrt{2\kappa\beta}/6; \qquad \kappa = \beta \xi^2/8. \tag{27}$$

With the aid of the Cahn–Hilliard model, the expression of surface tension force applied in Eqs. (12)–(14) can be written as:

$$\mathbf{F}_s = (F_{sx}, F_{sy}) = -C\nabla\mu. \tag{28}$$

In this work, Eq. (23) is solved by the finite difference scheme. In particular, the convective term $\nabla \cdot (\boldsymbol{u}C)$ is discretized by the fifth-order Weighted Essentially Non-Oscillatory scheme (WENO) [35] and the diffusive term is approximated by the central difference scheme. For regular domain with uniform grid, the WENO scheme and the central difference scheme are applied directly in the Cartesian coordinate system. For curved boundary and non-uniform grids, Eq. (23) is transformed to the form in the curvilinear coordinate system (computational space) first by using the body-fitted coordinate transformation. As uniform mesh is used in the computational space, the conventional WENO scheme [35] and the central difference scheme are applied to discretize relevant convective and diffusive terms. As an example, the convective term $\nabla \cdot (\boldsymbol{u}C)$ is taken to illustrate the process. With coordinate transformation from the physical space (x, y) to the computational space (ξ, η), $\nabla \cdot (\boldsymbol{u}C)$ can be written in the computational space as,

$$\nabla \cdot (\boldsymbol{u}C) = \frac{1}{J}\left[\frac{\partial}{\partial \xi}\widehat{F} + \frac{\partial}{\partial \eta}\widehat{G}\right] \tag{29}$$

where $\widehat{F} = \frac{\partial y}{\partial \eta}(uC) - \frac{\partial x}{\partial \eta}(vC)$, $\widehat{G} = -\frac{\partial y}{\partial \xi}(uC) - \frac{\partial x}{\partial \xi}(vC)$ and $J = \frac{\partial y}{\partial \eta}\frac{\partial x}{\partial \xi} - \frac{\partial y}{\partial \xi}\frac{\partial x}{\partial \eta}$. For numerical discretization, the first order derivatives of $\widehat{F}$ and $\widehat{G}$ in Eq. (29) can be approximated by the WENO scheme [35] on the uniform mesh (in the computational space). The above process is also applicable to the diffusive term.

When a solid wall is encountered in the multiphase flow, numerical solution of Eq. (23) needs two physical boundary conditions for interactions between the wall and fluids. Firstly, to ensure the mass conservation law, the boundary condition for $\nabla^2 \mu_C$ at wall is given by the chemical potential gradient:

$$\boldsymbol{n} \cdot \nabla \mu|_{wall} = 0, \tag{30}$$

where $\boldsymbol{n}$ is the unit outer normal vector. Secondly, to minimize the total free energy contributed to the specified wall free energy, the boundary condition for $\nabla^2 C$ are applied [21]:

$$\boldsymbol{n} \cdot \nabla C|_{wall} = \omega\left(C_{wall} - C_{wall}^2\right)\sqrt{2\beta/\kappa}, \tag{31}$$

where ω is the non-dimensional wetting potential determined by Young's Law. The equilibrium contact angle θ^{eq} at the three phase contact line can be computed by:

$$\cos\theta^{eq} = -\omega. \tag{32}$$

The contact angle θ^{eq} is determined by the material properties of the fluids and solid wall and can be given in advance.

2.3. Computational procedure

The overall computational procedure of the present MLBFS for simulation of multiphase flows is summarized as follows:

(1) Firstly, specify the streaming distance δ_x $(\delta_x = \delta_t)$ at each interface. As shown in Fig. 2, the constraint that the location of $(\boldsymbol{r} - \boldsymbol{e}_\alpha \delta_t)$ should be within either the cell Ω_i or the cell Ω_{i+1} must be satisfied;
(2) For any considered interface position $\boldsymbol{r}$, calculate ρ, $\boldsymbol{u}$ and p at $(\boldsymbol{r} - \boldsymbol{e}_\alpha \delta_t)$ using Eq. (19) and further compute $f_\alpha^{eq}(\boldsymbol{r} - \boldsymbol{e}_\alpha \delta_t, t - \delta_t)$ using Eq. (3);
(3) Obtain ρ, $\boldsymbol{u}$ and p at the cell interface using Eqs. (20)–(22), and further calculate $f_\alpha^{eq}(\boldsymbol{r}, t)$;
(4) Calculate the single relaxation parameter τ using Eq. (17);
(5) Calculate f_α^{neq}, and $f_\alpha^{\wedge}$ by using Eqs. (18) and (15a) respectively;
(6) Compute the tensor Π^e using Eq. (9) and the source terms in Eq. (14);
(7) Evaluate the fluxes $\boldsymbol{R}_k$ at the cell interface by Eq. (16);
(8) Discretize Eq. (23) using the WENO scheme;
(9) Apply the 3rd order TVD Runge–Kutta temporal scheme to solve Eqs. (13) and (23);
(10) Repeat steps (2–9) until converged solutions are obtained.

3. Numerical results and discussion

In this section, the MLBFS is validated by simulating several benchmark test cases. First, the two-phase co-current flow with density ratio up to 1000 in a channel is simulated. The obtained results are compared with the analytical solutions. Secondly, the flow of droplet spreading on a flat plate is simulated to examine the reliability of the MLBFS with complicated boundary conditions. After that, to further examine the MLBFS for unsteady multiphase flows, the Rayleigh–Taylor instability is investigated. This flow will be studied at both low and high Reynolds numbers. The fourth test case is droplet splashing on a thin film with density ratio of 1000. This problem is studied to examine the performance of the present solver for high-density-ratio multiphase flows.
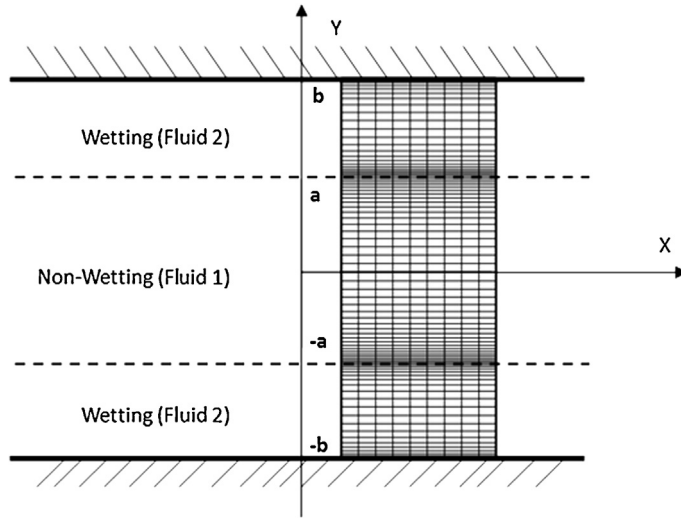
Fig. 3. Configuration and computational grid of the two-phase co-current flows.

3.1. Immiscible two-phase co-current flow in a 2D channel

The co-current flow in a 2D channel driven by an external force F_x is considered. The configuration and non-uniform computational mesh of this flow are displayed in Fig. 3. In this figure, the non-wetting fluid 1 of density ρ_L is placed in the region $|y| < a$ of the channel while the wetting fluid 2 of density ρ_H is within $a \leq |y| < b$. Fine grids around the phase interface and near the wall are adopted. The analytical solutions of this flow can be found in [36,37].

Firstly, to examine the accuracy of the present solver, the flows at four different density ratios of $R_\rho = \rho_H/\rho_L = 10$, 20, 100 and 1000 are considered. The flow parameters are set as: $\nu_1 = \nu_2 = 0.01$, $a = 50$, $b = 100$, $\rho_H = 1$ and $F_x = 1 \times 10^{-9}$. The external force F_x is exposed on either Fluid 1 or Fluid 2. A fine non-uniform grid size of 50×200 is applied for these four cases. Figs. 4 and 5 show the velocity profiles for cases of the external force being exposed respectively on Fluid 1 and Fluid 2. Also included are the analytical solutions. It is seen that the present results agree excellently well with those analytical solutions, which successfully validates the reliability of the present solver.

After that, we further examine its efficiency. A density ratio of $R_\rho = 10$ is considered and the flow parameters are set the same as those in the previous cases. Three non-uniform grid sizes of 41×11, 81×11 and 121×11 and one uniform grid size of 121×11 are applied. Numerical simulations are carried out on Lenovo Laptop (Intel I3 core with 2.53 GHz and 4 GB RAM). The time step is set locally for each simulation case. The maximum horizontal velocity $U_{\max}$ and the computational time on different grids are compared in Table 1. It can be seen that, the relative error between the present result obtained on a non-uniform grid size of 81×11 and analytical solution is 1.33%, which is lower than 2.01% obtained on the uniform grid size of 121×11. The computational time for the grid size of 81×11 is 547.9 s, which is improved by 62.6% as compared with that of 1465.2 s on the uniform grid size of 121×11. Even for the same grid size of 121×11, the computational time for non-uniform grid is much less than that for uniform grid due to the use of local time step.

### 3.2. Two-phase Taylor–Couette flows in two concentric cylinders

To further display the capability of the present solver for flows with curved boundary, the two-phase Taylor–Couette flow is considered. The schematic diagram and typical body-fitted grid for this problem are depicted in Fig. 6. Two layers of fluids are filled in the annulus. The inner cylinder of radius R_1 is rotating with angular velocity ω while the outer cylinder of radius R_2 is kept stationary. The interface is located at the middle of the annulus, which forms a circle with radius R_i. The dynamic viscosity of Fluid 1 and Fluid 2 and their ratio are denoted respectively as μ_1, μ_2 and $M_{\mu_2/\mu_1} = \mu_2/\mu_1$.

In the present study, the geometrical and flow parameters are set as: $R_1 = 1$, $R_2 = 2$, $R_i = 1.5$ and $\omega = 0.05$. With these parameters, the analytical solutions for this problem at low Reynolds number can be given as follows:

$$u_\theta = \begin{cases} A_1 r + B_1/r, & r < 1.5 \\ A_2 r + B_2/r, & r > 1.5 \end{cases} \tag{33}$$

where $A_1 = (7 - 16M)\omega/(20M + 7)$, $B_1 = 36\omega M/(20M + 7)$, $A_2 = -9\omega/(20M + 7)$ and $A_2 = 36\omega/(20M + 7)$. Three different viscosity ratios of $M_{\mu_2/\mu_1} = 1$, 2 and 10 are tested and a grid size of 81×81 is applied. The no-slip boundary conditions are applied on the cylinder surfaces in the same way as those in N–S solvers. Fig. 7 compares the numerical results with the analytical solution. Obviously, good agreements have been achieved, which demonstrates one of the advantages of MLBFS, that is, flexible for application on non-uniform mesh.
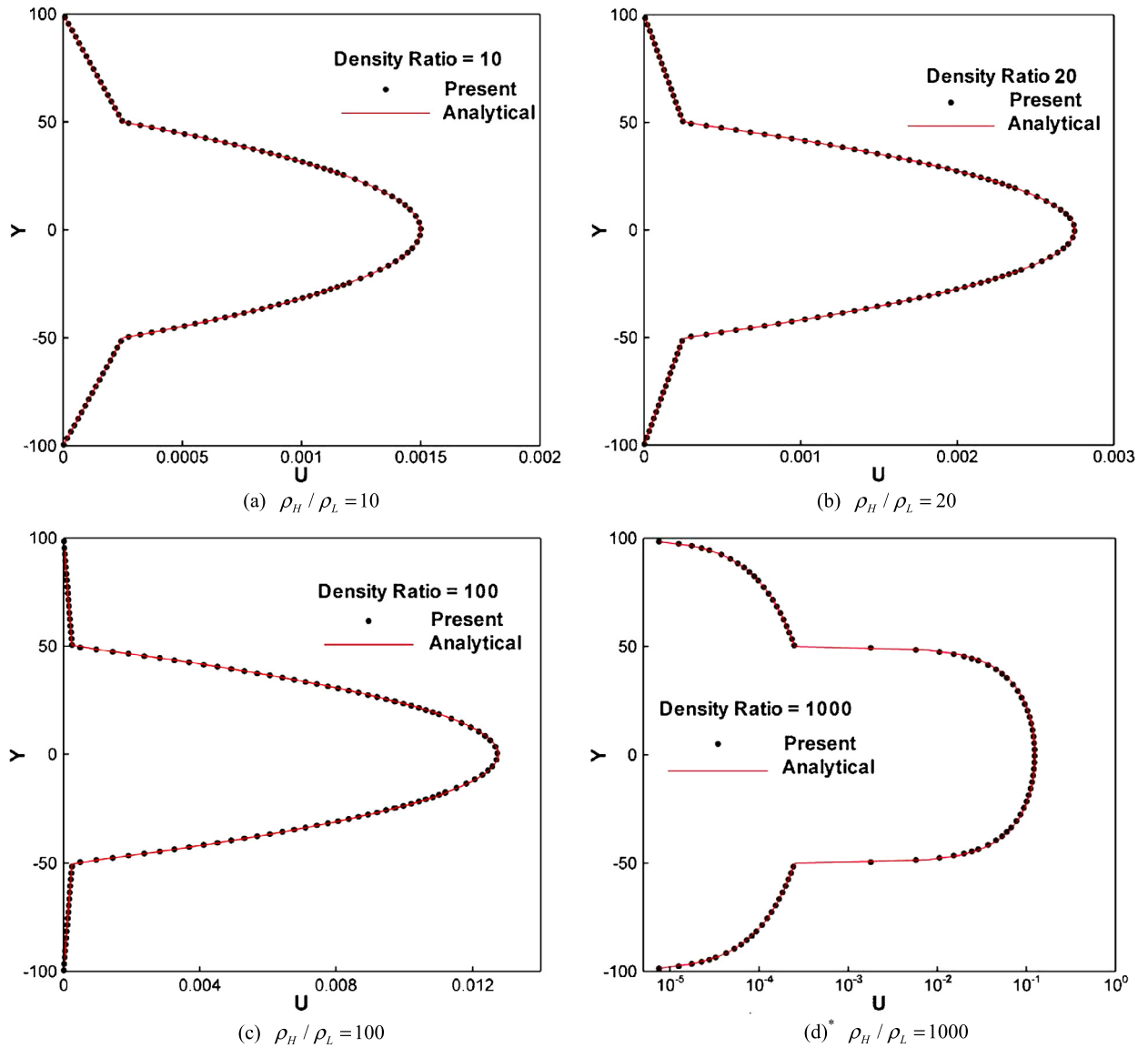
Fig. 4. Velocity profiles of the two-phase co-current flows with $\rho_H/\rho_L = 10, 20, 100$ and 1000: forces on Fluid 1 (*Note that the velocity in panel (d) is shown in the log scale due to its very small value in the wetting region).

3.3. Droplet spreading on a flat plate

In this section, we further examine how to implement the wetting condition in the MLBFS. First, the no-slip boundary condition should be applied on the wall. Besides, Eqs. (29)–(30) should be implemented when solving the Cahn–Hilliard equation. Actually, the wetting condition is controlled by the non-dimensional wetting potential ω in Eqs. (31).

In our simulations, a rectangular domain with a grid size of 200×100 is used. A horizontal wall is placed on the bottom of the computational domain. The densities of liquid and gas are $\rho_H = 1.0$, $\rho_L = 0.1$, the interface thickness is $\xi = 3$ lattice unit and the surface tension is $\sigma = 0.001$. A liquid droplet with radius of 25 lattice units is generated at the center of the plate. Due to surface tension and the adhesion force between fluids and the wall, at beginning, the contact point moves and the droplet deforms. When the droplet reaches an equilibrium state, the contact angle θ^{eq} becomes constant. Through specifying different ω, four different contact angles of $\theta^{eq} = 30°, 90°, 120°$ and $150°$ can be obtained as shown in Fig. 9. Through measuring the equilibrium contact angles using a geometric formula, the measured contact angles are compared with analytical ones in Fig. 8. It is seen that the contact angles obtained from MLBFS agree well with the theoretical predictions.
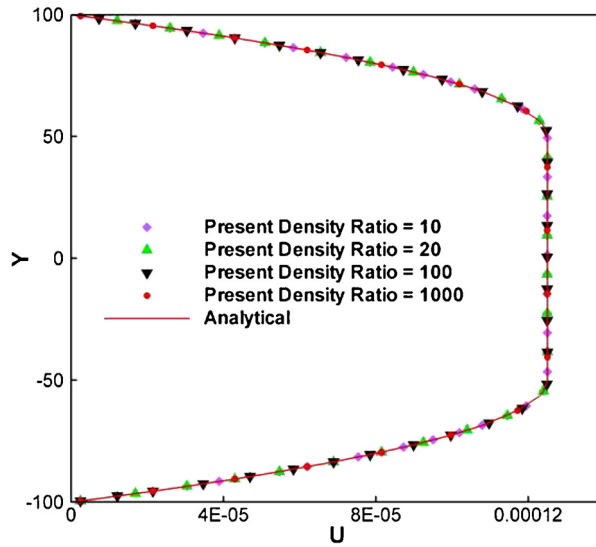
Fig. 5. Velocity profiles of the two-phase co-current flows with $\rho_H/\rho_L = 10, 20, 100$ and 1000: forces on Fluid 2.

Table 1
Comparison of computational efficiency on different grids for the co-current flows at density ratio of 10.

Grid		U_{max}		Relative error (%)	CPU time (s)
		Present	Analytical		
Non-uniform	41×11	0.001452		3.2	128.1
	81×11	0.001480	0.0015	1.33	547.9
	121×11	0.001487		0.86	907.1
Uniform	121×11	0.001469		2.01	1465.2

(a)   (b)
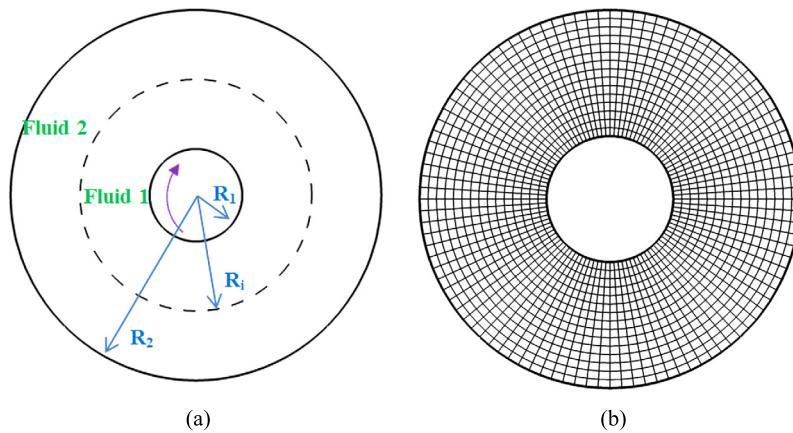
Fig. 6. Schematic diagram and typical computational mesh of the two-phase Taylor–Couette flows.

3.4. Rayleigh–Taylor instability

The Rayleigh–Taylor instability of binary fluids under gravity involves very interesting phenomenon and has been investigated extensively by many researchers [17,38–44]. This benchmark case is also simulated here to test the proposed MLBFS.

Consider a rectangular box of $\Omega = [-d/2, d/2] \times [-2d, 2d]$ filled with two layers of fluids, heavy fluid (density ρ_H) on top of light one (density ρ_L). This box is exposed under gravity. Periodic boundary conditions are applied to the left and right boundaries. The wall boundary conditions are applied to the upper and lower boundaries. Initially, a perturbation is generated through specifying the position of interface $y(x) = 0.1d \cos(2\pi x/d)$. Two non-dimensional parameters of this problem can be defined based on the characteristic length d and time $T = \sqrt{d/g}$: the Reynolds number $\text{Re} = \sqrt{dg} \cdot d/\nu$ and the Atwood number $At = (\rho_H - \rho_L)/(\rho_H + \rho_L)$. The kinematic viscosity ν is identical for two fluids. The following parameters
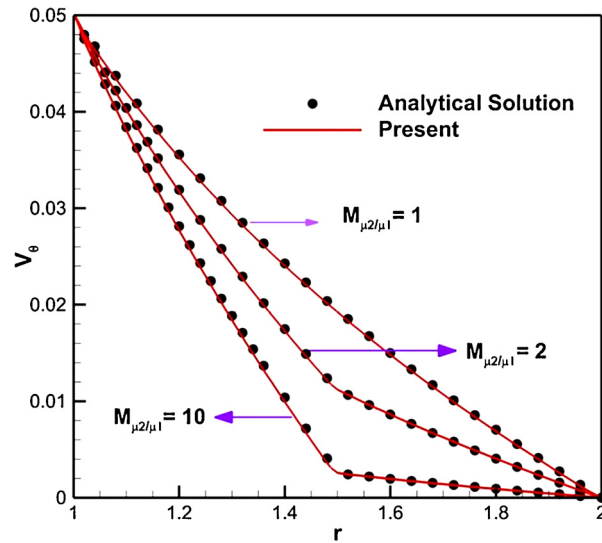
Fig. 7. Comparison of azimuthal velocity u_θ along the symmetric axis for the two-phase Taylor–Couette flows with different viscosity ratio.
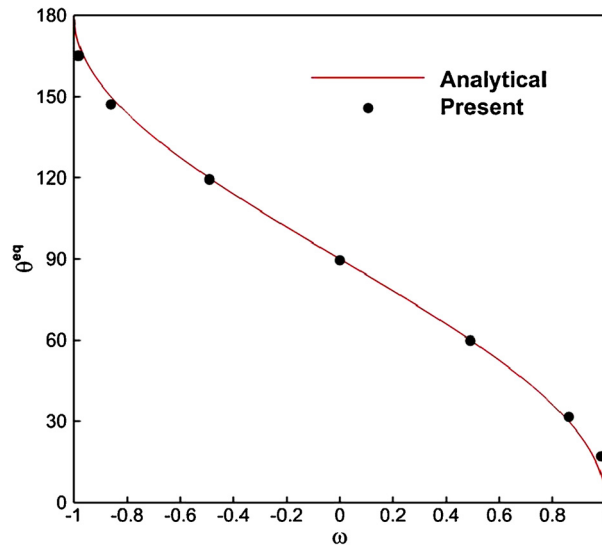

Fig. 8. Comparison of the equilibrium contact angles between the present results and the analytical data.

are applied for simulations: $d = 200$, $\sqrt{dg} = 0.01$, $At = 0.5$ and $\rho_L = 1$. A grid size of 200×800 is applied. In present study, cases of Re = 256 and 3000 are simulated.

For the case of Re = 256, the interface positions and velocities of bubble front of light fluid and spike tip of heavy fluid are plotted in Fig. 10 respectively. Also included in these figures are the results obtained by the conventional LB solver of He et al. [17] and Navier–Stokes solver of Nourgaliev et al. [43] for comparison. It can be seen that the present solutions lay between those of Refs. [17] and [43]. The evolutions of the interface at different times are illustrated in Fig. 12, where 19 equally spaced density contours are plotted in each picture. At early time, the falling spike of heavy fluid and rising bubble of light fluid are formed. After initial evolution, two counter-rotating vortices are generated adjacent to the falling spike due to the rolling-up of the heavy fluid. As the evolution continues, these two vortices are slough off and a pair of secondary vortices are formed at the tails of the roll-ups. The roll-ups and secondary vortices can be explained by the Kelvin–Helmholtz instability [40]. All these observations agree well with those in the literature [17,38–41].

For the case of Re = 3000, the simulation is more challenging because the convective terms in the N–S equations dominate the flow and may encounter numerical instability. We try to simulate this problem at high Reynolds number to verify the capability of MLBFS. The present numerical results of the interface positions at Re = 3000 are shown in Fig. 11. The Navier–Stokes solutions of Ding et al. [44] by using the high order WENO scheme and those of Guermond and Quartapelle [41] by applying a projection FEM are also included for comparison. Good agreements are reached among the results. The instantaneous patterns of the interface positions at different time are displayed in Fig. 13. Similar phenomenon, like roll-
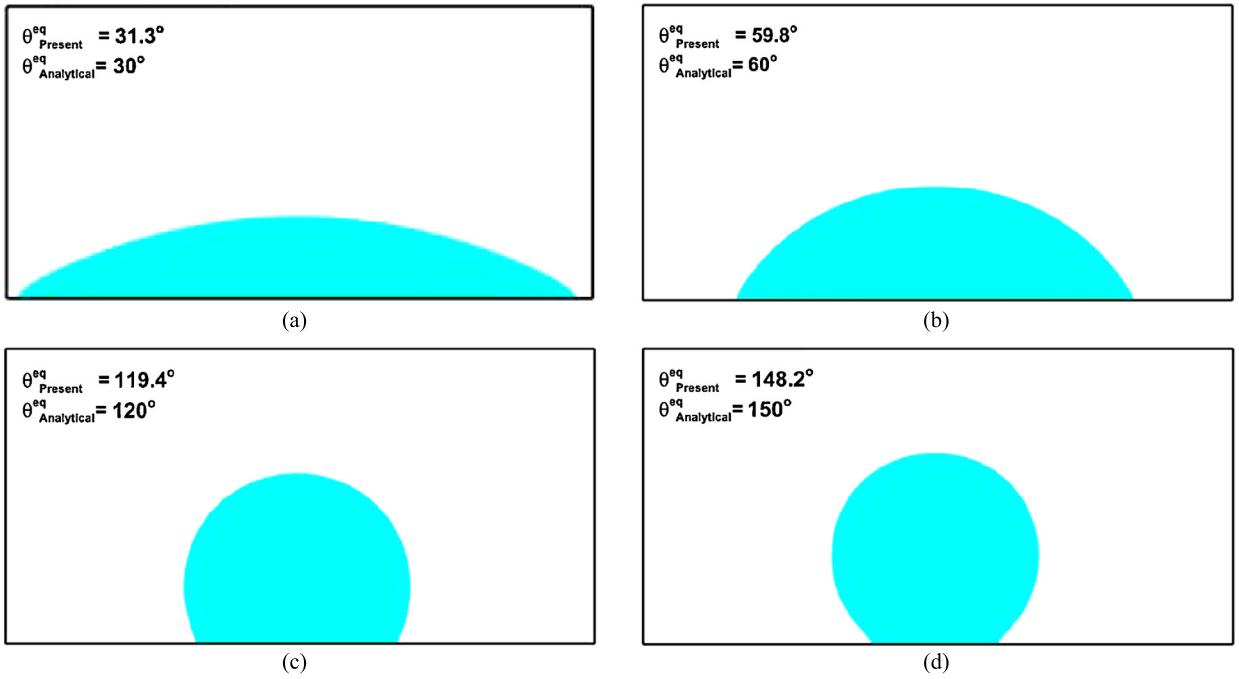
Fig. 9. Four different equilibrium contact angles obtained by the MLBFS.
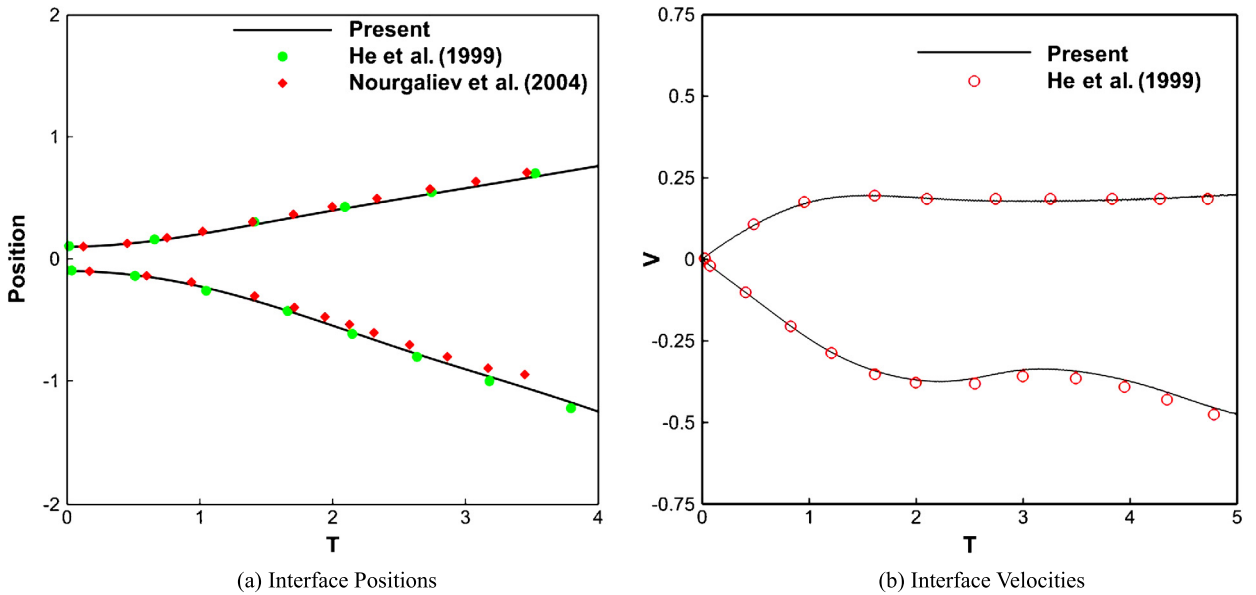

(a) Interface Positions　　　　(b) Interface Velocities

Fig. 10. Positions and velocities of the bubble and spike fronts for the Rayleigh–Taylor instability at Re = 256.

ups and secondary vortices at low Reynolds number of 256, can be clearly observed. These comparisons and observations validate the reliability of the present solver for multiphase flows at high Reynolds numbers.

3.5. Droplet splashing on a thin film

In this section, the problem of a droplet splashing on a thin film is investigated to further validate the present solver for multiphase flows with large density ratio and high Reynolds numbers. Previous studies of this problem [45–47] show that, when splashing occurs, the impact radius defined in [45] obeys a power law. This law will be used to further validate our scheme.
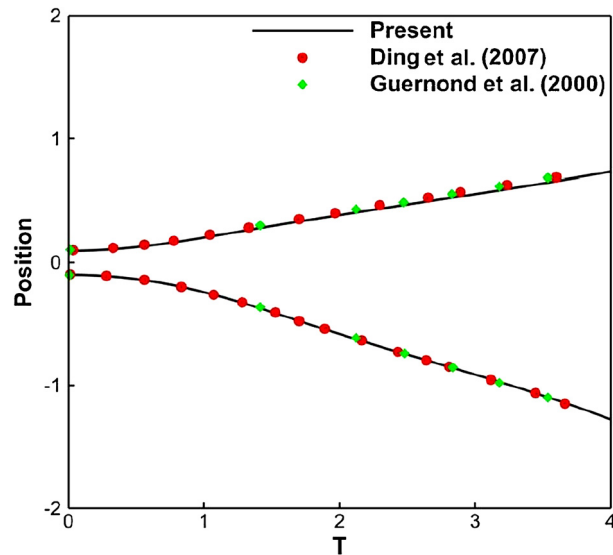
Fig. 11. Positions of interfaces for the Rayleigh–Taylor instability at Re = 3000.

The schematic diagram of this problem is depicted in Fig. 14, which shows a liquid droplet moving downward with velocity U to a thin film in an ambient vapor field. The radius of the droplet and the height of the thin film are given respectively as R and H. The density and viscosity of the liquid droplet and vapor are noted respectively as (ρ_H, μ_H) and (ρ_L, μ_L). This problem can be normalized by two non-dimensional parameters: the Reynolds number $Re_H = 2\rho_H U R/\mu_H$ and the Weber number $We_H = 2\rho_H U^2 R/\sigma$, where σ is the surface tension. Since the flow is symmetric, the computational domain in present study only involves half of the flow field to reduce the computational cost. The flow parameters are set as $U = 0.004$, $R = 100$, $\rho_H = 1$ in lattice units, and $\rho_H/\rho_L = 1000$, $\mu_H/\mu_L = 40 We_H = 2000$.

At first, a grid independence study is carried out on three different grids of 251×501, 376×751 and 501×1001 for this problem at Re = 500. Fig. 15 shows the liquid–gas interfaces at $T = 1$. As shown in the figure, the interfaces obtained on the finest grid of 501×1001 coincide well with those obtained on the grid of 376×751 except for a small fraction near the finger tip of the splashing fluid. This indicates that the grid of 501×1001 is fine enough to capture the interface details for this case.

After that, numerical simulations of this problem at six different Reynolds numbers of 20, 100, 200, 400, 500 and 1000 are carried out to demonstrate the performance of the present solver for multiphase flows at large density ratio and high Reynolds number. The evolutions of the instantaneous interface positions for Re = 20, 100, 400 and 1000 are shown in Figs. 16–19 respectively. When the Reynolds number is low (Re = 20), an outward-moving surface wave can be observed from Fig. 16, which is also known as a deposition process. The splashing is not formed in this case. As the Reynolds number is increased to 100, a liquid sheet coming out of the neck is observed from Fig. 17. Two liquid fingers at the end rim of the splashing are generated after the impact of the droplet. These liquid fingers are strong enough to withstand the surface tension force and viscous force so that instability or breakup of the splashing liquids does not occur at this Reynolds number. As Re = 400, similar splashing phenomenon can be observed from Fig. 18 as those at Re = 100. However, the thickness of the fingers becomes smaller and instability occurs at the end rim of the liquid sheets. As Re is further increased to 1000, two liquid fingers at the end rim of the splashing shown in Fig. 19 become even thinner, which forms a thin film in the direction perpendicular to the plane. At $T = 1.2$, a tiny liquid droplet can be observed near the end rim of the liquid fingers. At $T = 2$, due to effects of the surface tension force and viscous force, these fingers are so instable that a breakup occurs at the end rim of the liquid sheet. It can also be seen from Figs. 16–19 that the interface curve in the middle part is disappeared after some time. The reason may be that air entrainment phenomenon occurs in a narrow region between the droplet and the thin film immediately after the impact of droplet on the liquid film. As the impact continues, the narrow zone occupied by air gets thinner and thinner since the air is being drained out from the neck of the region. This phenomenon has also been found experimentally in [48]. As the impact continues further, some air is entrapped in a much narrower region and/or scattered zone. The scale of the entrapped air, which is comparable or smaller than the interface thickness, is so small that it is not visible (disappear). This can also be found in the reference of Lee and Lin [20]. As pointed out in [44], this is a common feature that the DIM (diffuse interface method) restricts its ability in resolving small interfacial structures whose scale is comparable to the interface thickness.

To quantify the present results, the non-dimensional impact radius $r/(2R)$ is examined, the definition of which is given in Ref. [45]. Previous studies [45,46] show that the impact radius generally follows the power law $r/(2R) \approx \alpha\sqrt{Ut/2R}$, where the constant α is about 1.0 according the theoretical predictions [45]. The present results of the impact radius are depicted in Fig. 20 as a function of non-dimensional time $Ut/2R$. As can be seen, the present numerical results agree well with the prediction of the power law $r/(2R) \approx \sqrt{Ut/2R}$.
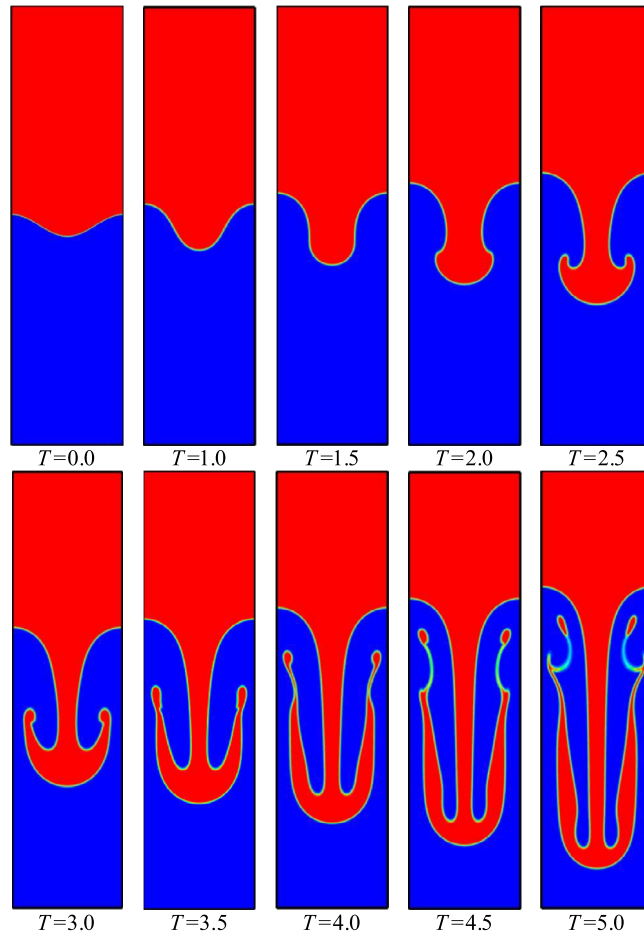
Fig. 12. Evolution of the fluid interface for the Rayleigh–Taylor instability at Re = 256.

4. Conclusions

This paper presents a multiphase lattice Boltzmann flux solver (MLBFS) for effective simulation of incompressible multiphase flows with large density ratio and high Reynolds number. The MLBFS applies the finite volume method to solve the N–S equations. Both the viscous and inviscid fluxes are evaluated in a simple and easy way at the cell interface by the local reconstruction of the LBE solutions. The external forcing terms are handled directly in the solver. Due to the local application of the LBM and the finite volume method, the present solver has the following advantages: (1) it retains the advantages of the standard LBM in the flux reconstruction process; (2) it can be effectively applied on non-uniform grids with more stable temporal schemes while the conventional multiphase LB model restricts its applications on uniform grids with fixed time step; (3) it has a much simpler and more straightforward way to deal with external forcing terms and boundary conditions.

The MLBFS has been validated through several numerical tests of the two-phase co-current flows with density ratio up to 1000, two-phase Taylor–Couette flows in an annulus, Rayleigh–Taylor instabilities at the Reynolds number of 256 and 3000, and droplet splashing on a thin film at density ratio of 1000 with a Reynolds number ranging from 20 to 1000. Good agreements have been achieved between the MLBFS solutions and benchmark data published in the literature. The good agreements verify the reliability of the MLBFS for simulation of multiphase flows with large density ratio and high Reynolds number. The capability of the MLBFS for applications on non-uniform grids is also demonstrated.

Appendix A. Chapman–Enskog expansion analysis

By introducing multi-scale expansion, the density distribution function, the temporal derivative and the spatial derivative can be expanded respectively as

$$f_\alpha = f_\alpha^{(0)} + \varepsilon f_\alpha^{(1)} + \varepsilon^2 f_\alpha^{(2)}, \tag{A.1a}$$
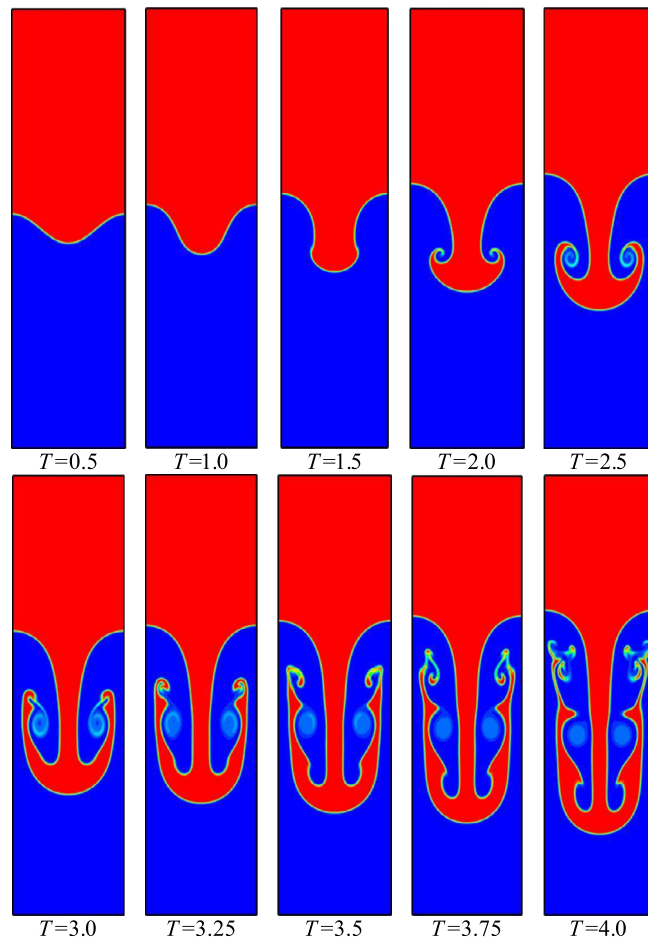
Fig. 13. Evolution of the fluid interface for the Rayleigh–Taylor instability at Re = 3000.
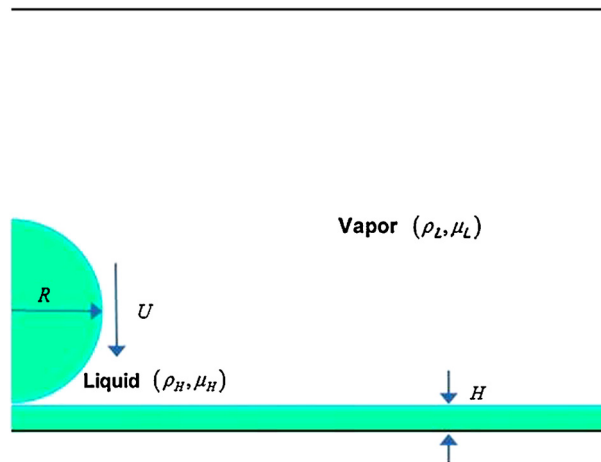

Fig. 14. Schematic diagram of the droplet splashing on a thin film.

$$\frac{\partial}{\partial t} = \varepsilon \frac{\partial}{\partial t_0} + \varepsilon^2 \frac{\partial}{\partial t_1},$$
(A.1b)

$$\nabla_r = \varepsilon \nabla_{r1},$$
(A.1c)

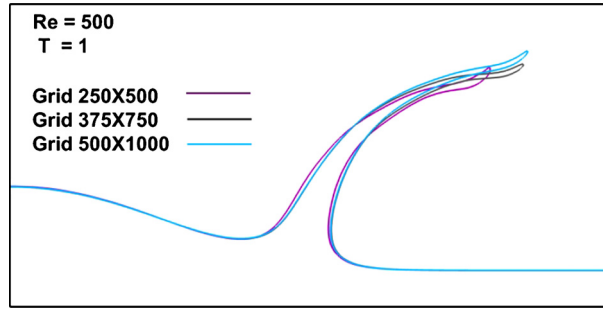where ε is a small parameter proportional to the Knudsen number.

Fig. 15. Grid independence study for the droplet splashing on a thin film at Re = 500.
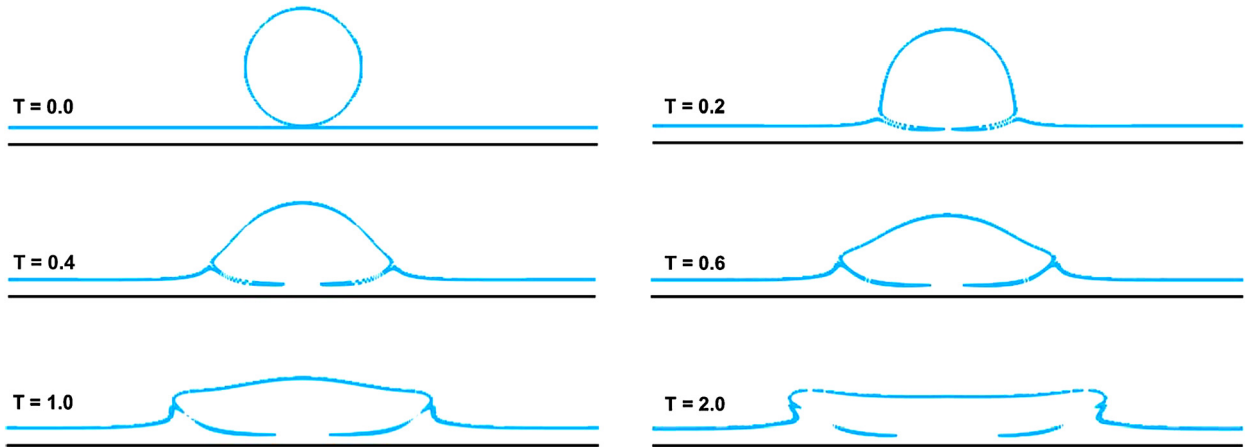

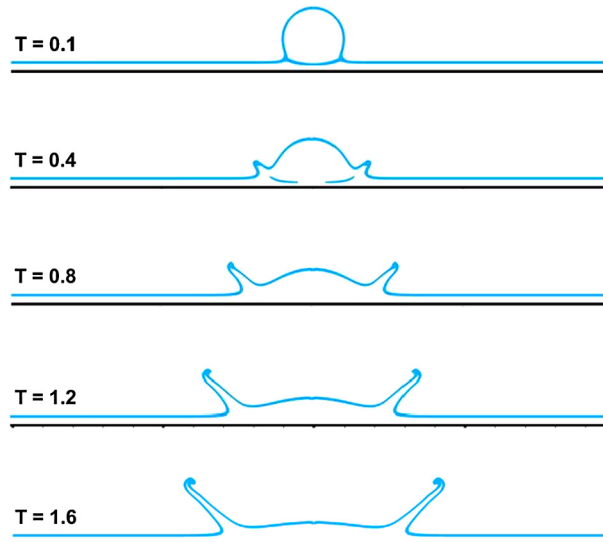**Fig. 16.** Evolution of the instantaneous interface for the droplet splashing on a thin film at Re = 20.

Fig. 17. Evolution of the instantaneous interface for the droplet splashing on a thin film at Re = 100.

By performing Taylor series expansion in time and space for Eq. (2), the following differential equation with the second order of accuracy is obtained,

$$\left(\frac{\partial}{\partial t} + \boldsymbol{e}_\alpha \cdot \nabla\right) f_\alpha + \frac{\delta_t}{2}\left(\frac{\partial}{\partial t} + \boldsymbol{e}_\alpha \cdot \nabla\right)^2 f_\alpha + \frac{1}{\tau \delta_t}\left(f_\alpha - f_\alpha^{eq}\right) + O\left(\delta_t^2\right) = 0. \tag{A.2}$$
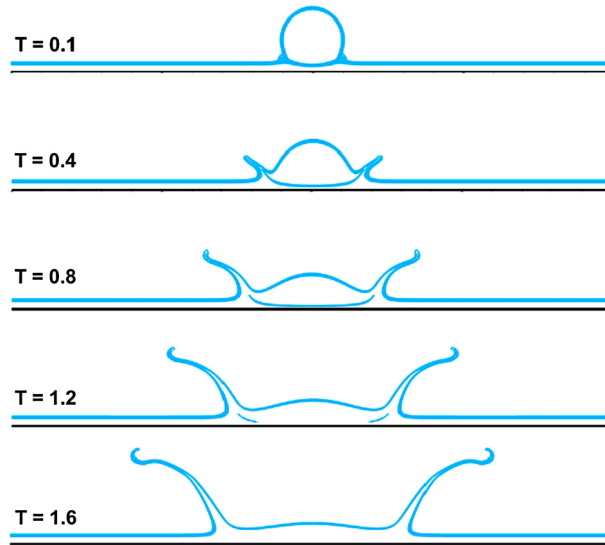
Fig. 18. Evolution of the instantaneous interface for the droplet splashing on a thin film at Re = 400.
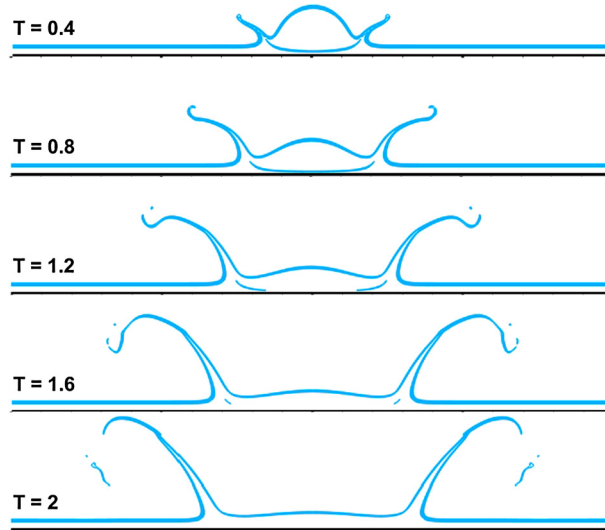

Fig. 19. Evolution of the instantaneous interface for the droplet splashing on a thin film at Re = 1000.

Substituting Eq. (A.1) into Eq. (A.2) gives the following three equations in terms of ε order,

$$O(\varepsilon^0): \quad (f_\alpha^{(0)} - f_\alpha^{eq})/(\tau \delta_t) = 0, \tag{A.3}$$

$$O(\varepsilon): \quad \frac{D}{Dt_0} f_\alpha^{(0)} + \frac{1}{\tau \delta_t} f_\alpha^{(1)} = 0, \tag{A.4}$$

$$O(\varepsilon^2): \quad \frac{\partial f_\alpha^{(0)}}{\partial t_1} + \left(1 - \frac{1}{2\tau}\right) \frac{D}{Dt_0} f_\alpha^{(1)} + \frac{1}{\tau \delta_t} f_\alpha^{(2)} = 0, \tag{A.5}$$

where $\frac{D}{Dt_0} = (\frac{\partial}{\partial t_0} + \mathbf{e}_\alpha \cdot \nabla_1)$.

By taking summation of Eqs. (A.4) and (A.5) over α, the following equations on the t_0 and t_1 time scales can be derived:

$$\frac{\partial p}{\partial t_0} + \nabla_1 \cdot \left(\sum_{\alpha=0}^{N} \mathbf{e}_\alpha f_\alpha^{eq}\right) = 0, \tag{A.6}$$

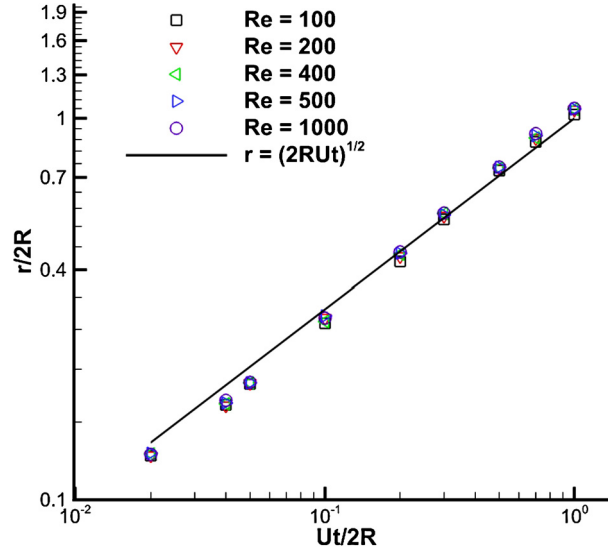$$\frac{\partial p}{\partial t_1} = 0. \tag{A.7}$$

Fig. 20. The predicted spread radius at different Reynolds numbers for droplet splashing on a thin film with density ratio of 1000.

Similarly, by taking the first-moment summation of Eqs. (A.4) and (A.5) over α, the resultant equations on the t_0 and t_1 time scales can be written as:

$$\frac{\partial \rho c_s^2 \boldsymbol{u}}{\partial t_0} + \nabla_1 \cdot \Pi^{(0)} = 0, \tag{A.8}$$

$$\frac{\partial \rho c_s^2 \boldsymbol{u}}{\partial t_1} + \left(1 - \frac{1}{2\tau}\right)\nabla_1 \cdot \Pi^{(1)} = 0, \tag{A.9}$$

where

$$\Pi_{jk}^0 = \sum_{\alpha=0}^{N} (\boldsymbol{e}_\alpha)_j (\boldsymbol{e}_\alpha)_k f_\alpha^{eq}; \qquad \Pi_{jk}^{(1)} = -\tau \delta_t \sum_{\alpha=0}^{N} (\boldsymbol{e}_\alpha)_j (\boldsymbol{e}_\alpha)_k \frac{D}{Dt_0} f_\alpha^{eq}. \tag{A.10}$$

Combining the resultant formulations of (A.6) and (A.7) on the t_0 and t_1 time scales, the pressure evolution equation is derived

$$\frac{\partial p}{\partial t} + \nabla \cdot \left(\sum_{\alpha=0}^{N} \boldsymbol{e}_\alpha f_\alpha^{eq}\right) = 0. \tag{A.11}$$

Furthermore, combining the resultant formulations on the t_0 and t_1 time scales, the following momentum equation is obtained:

$$\frac{\partial \rho c_s^2 \boldsymbol{u}}{\partial t} + \nabla \cdot \Pi = 0, \tag{A.12}$$

where Π is the momentum flux tensor defined by

$$\Pi_{jk} = \Pi^{(0)} + \left(1 - \frac{1}{2\tau}\right)\Pi^{(1)} = \sum_{\alpha=0}^{N} (\boldsymbol{e}_\alpha)_j (\boldsymbol{e}_\alpha)_k \left[f_\alpha^{eq} + \left(1 - \frac{1}{2\tau}\right)f_\alpha^{neq}\right], \tag{A.13}$$

$$f_\alpha^{neq} = -\tau \delta_t \left(\frac{\partial}{\partial t} + \boldsymbol{e}_\alpha \cdot \nabla\right) f_\alpha^{eq}. \tag{A.14}$$

To get the final expressions of the macroscopic governing equation defined by (A.12), the key issue is to determine Π. The details to obtain Π are given below.

According to the definition of f_α^{eq} in Eq. (3) and with the aid of the D2Q9 lattice velocity model, we can easily get its first and second moments:

$$\sum_{\alpha=0}^{N} \boldsymbol{e}_\alpha f_\alpha^{eq} = \rho c_s^2 \boldsymbol{u},$$ (A.15a)

$$\Pi_{jk}^0 = \sum_{\alpha=0}^{N} (\boldsymbol{e}_\alpha)_j (\boldsymbol{e}_\alpha)_k f_\alpha^{eq} = c_s^2 (p\delta_{jk} + \rho u_j u_k).$$ (A.15b)

The tensor $\Pi_{jk}^{(1)}$ on the time scale t_1 is

$$
\begin{aligned}
\Pi_{jk}^{(1)} &= -\tau \delta_t \sum_{\alpha=0}^{N} (\boldsymbol{e}_\alpha)_j (\boldsymbol{e}_\alpha)_k \left(\frac{\partial}{\partial t_0} + \boldsymbol{e}_\alpha \cdot \nabla_1 \right) f_\alpha^{eq} \\
&= -\tau \delta_t \left[\frac{\partial}{\partial t_0} \Pi_{j,k}^{(0)} + \nabla_1 \cdot \sum_{i=0}^{n} e_{i,j} e_{i,k} e_{i,l} f_i^{eq} \right]
\end{aligned}
$$ (A.15c)

The terms of $\frac{\partial}{\partial t_0}\Pi_{j,k}^{(0)}$ and $\nabla_1 \cdot \sum_{i=0}^{n} e_{i,j}e_{i,k}e_{i,l}f_i^{eq}$ are given by:

$$
\begin{aligned}
\nabla_1 \cdot \sum_{i=0}^{n} e_{i,j}e_{i,k}e_{i,l}f_i^{eq} &= \nabla_1 \cdot \rho \sum_{i=0}^{n} w_i e_{i,j}e_{i,k}e_{i,l}e_{i,m}u_m \\
&= c_s^4 \nabla_1 \cdot \rho \Delta_{jklm} u_m = c_s^4 \partial_{x_l} (\rho \delta_{jk}\delta_{lm} + \rho\delta_{jl}\delta_{km} + \rho\delta_{jm}\delta_{kl})u_m \\
&= \rho c_s^4 \left(\delta_{jk}\nabla_1 \cdot \boldsymbol{u} + \frac{\partial u_j}{\partial x_k} + \frac{\partial u_k}{\partial x_l} \right) + c_s^4 (\delta_{jk}u_l + \delta_{jl}u_k + \delta_{kl}u_j)\frac{\partial \rho}{\partial x_l},
\end{aligned}
$$

$$
\begin{aligned}
\frac{\partial}{\partial t_0}\Pi_{j,k}^{(0)} &= \frac{\partial}{\partial t_0}\left(pc_s^2\delta_{jk} + \rho u_j u_k c_s^2 \right) \\
&= c_s^2\delta_{jk}\frac{\partial}{\partial t_0}p + u_j\frac{\partial}{\partial t_0}\left(\rho c_s^2 u_k \right) + u_k\frac{\partial}{\partial t_0}\left(\rho c_s^2 u_j \right) - u_j u_k\frac{\partial}{\partial t_0}\left(\rho c_s^2 \right) \\
&= c_s^2\delta_{jk}\frac{\partial}{\partial t_0}p + u_j\left[-\frac{\partial}{\partial x_k}\left(pc_s^2 \right) - \frac{\partial}{\partial x_m}\left(\rho u_k u_m c_s^2 \right) \right] \\
&\quad + u_k\left[-\frac{\partial}{\partial x_j}\left(pc_s^2 \right) - \frac{\partial}{\partial x_m}\left(\rho u_j u_m c_s^2 \right) \right] - u_j u_k\frac{\partial}{\partial t_0}\left(\rho c_s^2 \right) \\
&= c_s^2\delta_{jk}\frac{\partial}{\partial t_0}p - c_s^2\left[u_j\frac{\partial}{\partial x_k}p + u_k\frac{\partial}{\partial x_j}p \right] - \frac{\partial}{\partial x_m}\left(\rho c_s^2 u_j u_k u_m \right) \\
&\quad - u_j u_k\frac{\partial}{\partial x_m}\left(\rho c_s^2 u_m \right) - u_j u_k\frac{\partial}{\partial t_0}\left(\rho c_s^2 \right) \\
&= c_s^2\delta_{jk}\left[-\rho c_s^2\nabla\cdot\boldsymbol{u} - c_s^2 u_m\frac{\partial \rho}{\partial x_m} \right] - c_s^2\left[u_j\frac{\partial}{\partial x_k}p + u_k\frac{\partial}{\partial x_j}p \right] - \frac{\partial}{\partial x_m}\left(\rho c_s^2 u_j u_k u_m \right) \\
&= -\rho c_s^4\delta_{jk}\nabla_1\cdot\boldsymbol{u} - \delta_{jk}c_s^4 u_m\frac{\partial \rho}{\partial x_m} - c_s^2\left[u_j\frac{\partial}{\partial x_k}p + u_k\frac{\partial}{\partial x_j}p \right] - \frac{\partial}{\partial x_m}\left(\rho c_s^2 u_j u_k u_m \right)
\end{aligned}
$$

With the low Mach number approximations, high order terms of $o(Ma^3)$, such as $\frac{\partial}{\partial x_m}(\rho c_s^2 u_j u_k u_m)$, can be neglected. Then, by combining $\frac{\partial}{\partial t_0}\Pi_{j,k}^{(0)}$ and $\nabla_1 \cdot \sum_{i=0}^{n} e_{i,j}e_{i,k}e_{i,l}f_i^{eq}$, the final expressions of $\Pi^{(1)}$ can be given by

$$\Pi_{jk}^{(1)} = -\tau\delta_t\left[\rho c_s^4\left(\frac{\partial u_j}{\partial x_k} + \frac{\partial u_k}{\partial x_l} \right) - c_s^2\left(u_j\frac{\partial}{\partial x_k} + u_k\frac{\partial}{\partial x_j} \right)(p - \rho c_s^2) \right]$$ (A.16)

Hence, with the aid of Eqs. (A.15) and (A.16), the governing equations recovered by the lattice Boltzmann model can be written as:

$$\frac{\partial p}{\partial t} + \nabla\cdot\left(\rho c_s^2\boldsymbol{u} \right) = 0,$$ (A.17a)

$$\frac{\partial \rho\boldsymbol{u}}{\partial t} + \nabla(\rho\boldsymbol{u}\otimes\boldsymbol{u}) = -\nabla p + \nabla\left[\mu\left(\nabla\boldsymbol{u} + (\nabla\boldsymbol{u})^T - \Pi^e/c_s^2 \right) \right],$$ (A.17b)

where the dynamic viscosity $\mu = \rho c_s^2(\tau - 1/2)\delta_t$ and the error tensor is

$$\Pi_{jk}^e = \frac{1}{\rho}\left(u_j\frac{\partial}{\partial x_k} + u_k\frac{\partial}{\partial x_j} \right)(p - \rho c_s^2).$$ (A.17c)

References

[1] L.M. Pismen, Nonlocal diffuse interface theory of thin film and moving contact line, Phys. Rev. E 64 (2001) 021693.
[2] C.G. Koh, M. Luo, M. Gao, W. Bai, Modeling of liquid sloshing with constrained floating baffle, Comput. Struct. 122 (2013) 270–279.
[3] L. Scarbolo, D. Molin, P. Perlekar, M. Sbragaglia, A. Soldati, F. Toschi, Unified framework for a side-by-side comparison of different multicomponent algorithms: lattice Boltzmann vs. phase field model, J. Comput. Phys. 234 (2013) 263–279.
[4] G. Thommes, J. Becker, M. Junk, A.K. Vaikuntam, D. Kehrwald, A. Klar, K. Steiner, A. Wiegmann, A lattice Boltzmann method for immiscible multiphase flow simulations using the level set method, J. Comput. Phys. 228 (2009) 1139–1156.
[5] C.W. Hirt, B.D. Nichols, Volume of fluid (VOF) method for the dynamics of free boundaries, J. Comput. Phys. 39 (1989) 201–225.
[6] M. Sussman, P. Smereka, S. Osher, A level set approach for computing solutions to incompressible two-phase flow, J. Comput. Phys. 114 (1994) 146–159.
[7] G. Tryggvason, B. Bunner, A. Esmaeeli, A front tracking method for computations of multiphase flow, J. Comput. Phys. 169 (2001) 708–759.
[8] D. Jacqmin, Calculation of two-phase Navier–Stokes flows using phase-field modeling, J. Comput. Phys. 155 (1999) 96–127.
[9] D.M. Anderson, G.B. Mcfadden, A.A. Wheeler, Diffuse-interface methods in fluid mechanics, Annu. Rev. Fluid Mech. 30 (1998) 139–165.
[10] S. Chen, G. Doolen, Lattice Boltzmann method for fluid flows, Annu. Rev. Fluid Mech. 30 (1998) 329–364.
[11] C.K. Aidun, J.R. Clausen, Lattice-Boltzmann method for complex flows, Annu. Rev. Fluid Mech. 42 (2010) 439–472.
[12] K.N. Premnath, J. Abraham, Three-dimensional multi-relaxation time (MRT) lattice-Boltzmann models for multiphase flow, J. Comput. Phys. 224 (2007) 539–559.
[13] A.K. Gunstensen, D.H. Rothman, S. Zaleski, G. Zanetti, Lattice Boltzmann model of immiscible fluids, Phys. Rev. A 43 (1991) 4320–4327.
[14] X. Shan, H. Chen, Lattice Boltzmann model for simulating flows with multiple phases and components, Phys. Rev. E 47 (1993) 1815–1819.
[15] X. Shan, H. Chen, Simulation of nonideal gases and liquid–gas phase-transition by the lattice Boltzmann equation, Phys. Rev. E 49 (1994) 2941–2948.
[16] M. Swift, E. Orlandini, W.R. Osborn, J.M. Yeomans, Lattice Boltzmann simulations of liquid–gas and binary fluid systems, Phys. Rev. E 54 (1996) 5041–5052.
[17] X. He, S. Chen, R. Zhang, A lattice Boltzmann scheme for incompressible multiphase flow and its application in simulations of Rayleigh–Taylor instability, J. Comput. Phys. 152 (1999) 652–663.
[18] P. Yuan, L. Schaefer, Equations of state in a lattice Boltzmann model, Phys. Fluids 18 (2006) 042101.
[19] T. Inamuro, T. Ogata, S. Tajima, N. Konishi, A lattice Boltzmann method for incompressible two-phase flows with large density differences, J. Comput. Phys. 198 (2004) 16–47.
[20] T. Lee, C.L. Lin, A stable discretization of the lattice Boltzmann equation for simulation of incompressible two-phase flows at high density ratio, J. Comput. Phys. 206 (2005) 16–47.
[21] T. Lee, L. Liu, Lattice Boltzmann simulations of micron-scale drop impact on dry surfaces, J. Comput. Phys. 229 (2010) 8045–8063.
[22] H.W. Zheng, C. Shu, Y.T. Chew, A lattice Boltzmann model for multiphase flow with large density ratio, J. Comput. Phys. 218 (2006) 353–371.
[23] Y.Y. Yan, Y.Q. Zu, A lattice Boltzmann method for incompressible two-phase flows on partial wetting surface with large density ratio, J. Comput. Phys. 227 (2007) 763–775.
[24] A.J. Briant, A.J. Wagner, J.M. Yeomans, Lattice Boltzmann simulation of contact line motion: I. Liquid–gas systems, Phys. Rev. E 69 (2004), 031602-14.
[25] A.J. Briantt, J.M. Yeomans, Lattice Boltzmann simulation of contact line motion: II. Binary fluids, Phys. Rev. E 69 (2004) 031603.
[26] Y. Zhao, L.S. Fan, An interaction potential based lattice Boltzmann method with adaptive mesh refinement (AMR) for two phase flow simulation, J. Comput. Phys. 228 (2009) 6456–6478.
[27] M. Cheng, J. Lou, T.T. Lim, Motion of a vortex ring in a simple shear flow, Phys. Fluids 21 (2009) 081701.
[28] M. Cheng, J.S. Hua, J. Lou, Simulation of bubble–bubble interaction using a lattice Boltzmann method, Comput. Fluids 39 (2010) 260–270.
[29] H.H. Liu, Y.H. Zhang, A.J. Valocchi, Modeling and simulation of thermocapillary flows using lattice Boltzmann method, J. Comput. Phys. 231 (2012) 4433–4453.
[30] H.H. Liu, A.J. Valocchi, Y.Z. Zhang, Q.J. Kang, Lattice Boltzmann phase-field modeling of thermocapillary flows in a confined microchannel, J. Comput. Phys. 256 (2014) 334–356.
[31] C. Shu, Y. Wang, L.M. Yang, J. Wu, Lattice Boltzmann flux solver: an efficient approach for numerical simulation of fluid flows, Trans. Nanjing Univ. Aeronaut. Astronaut. 31 (2014) 1–15.
[32] Y. Wang, C. Shu, C.J. Teo, Thermal lattice Boltzmann flux solver and its application for simulation of incompressible thermal flows, Comput. Fluids 94 (2014) 98–111.
[33] Y. Wang, C. Shu, C.J. Teo, A fractional step axisymmetric lattice Boltzmann flux solver for incompressible swirling and rotating flows, Comput. Fluids 96 (2014) 204–214.
[34] C.W. Shu, S. Osher, Efficient implementation of essentially non-oscillatory shock-capturing schemes, J. Comput. Phys. 77 (1987) 439–471.
[35] X.D. Liu, S. Osher, T. Chan, Weighted essentially non-oscillatory schemes, J. Comput. Phys. 115 (1994) 200–212.
[36] H.B. Huang, J.J. Huang, X.Y. Lu, On simulations of high-density ratio flow flows using color-gradient multiphase lattice Boltzmann models, Int. J. Mod. Phys. C 24 (2013) 1350021.
[37] H.B. Huang, X.Y. Lu, Relative permeabilities and coupling effects in steady-state gas–liquid flow in porous media: a lattice Boltzmann study, Phys. Fluids 21 (2009), 092104-10.
[38] D.J. Holdych, D. Rovas, J.G. Georgiadis, R.O. Buckius, An improved hydrodynamics formulation for multiphase flow lattice Boltzmann models, Int. J. Mod. Phys. C 9 (1998) 1393–1404.
[39] D.H. Sharp, An overview of Rayleigh–Taylor instability, Physica D 12 (1984) 3–10.
[40] G. Tryggvason, Numerical simulations of the Rayleigh–Taylor instability, J. Comput. Phys. 75 (1988) 253–282.
[41] J.L. Guermond, L. Quartapelle, A projection FEM for variable density incompressible flow, J. Comput. Phys. 165 (2000) 167–188.
[42] B.J. Daly, Numerical study of two fluid Rayleigh–Taylor instabilities, Phys. Fluids 10 (1967) 297.
[43] R.R. Nourgaliev, T.N. Dinh, T.G. Theofanous, A pseudocompressibility method for the numerical simulation of incompressible multifluid flows, J. Comput. Phys. 30 (2004) 901–937.
[44] H. Ding, P.D.M. Spelt, C. Shu, Diffuse interface model for incompressible two-phase flows with large density ratios, J. Comput. Phys. 226 (2007) 2078–2098.
[45] C. Josserand, S. Zaleski, Droplet splashing on a thin liquid film, Phys. Fluids 15 (2003) 1650.
[46] H.Y. Kim, Z. Feng, J.H. Chun, Instability of a liquid jet emerging from a droplet upon collision with a solid surface, Phys. Fluids 12 (2000) 531.
[47] Q. Li, K.H. Luo, X.J. Li, Lattice Boltzmann modeling of multiphase flows at large density ratio with improved pseudopotential model, Phys. Rev. E 87 (2013) 053301.
[48] T. Tran, H.D. Meleprade, C. Sun, D. Lohse, Air entrainment during impact of droplets on liquid surface, J. Fluid Mech. 76 (2013) R3.